Batteries Hot Paper

Zitierweise: *Angew. Chem. Int. Ed.* **2021**, *60*, 19306–19313
Internationale Ausgabe: doi.org/10.1002/anie.202105831
Deutsche Ausgabe: doi.org/10.1002/ange.202105831

Current-Density Regulating Lithium Metal Directional Deposition for Long Cycle-Life Li Metal Batteries

*Heng Mao, Wei Yu, Zhuanyun Cai, Guixian Liu, Limin Liu, Rui Wen, Yaqiong Su, Huari Kou, Kai Xi, Benqiang Li, Hongyang Zhao, Xinyu Da, Hu Wu, Wei Yan and Shujiang Ding**

Abstract: *Uncontrolled dendrite formation in the high energy density of lithium (Li) metal batteries (LMBs) may pose serious safety risks. While numerous studies have attempted to protect separators, these proposed methods fail to effectively inhibit upward dendrite growth that punctures through the separator. Here, we introduce a novel „orientated-growth" strategy that transfers the main depositional interface to the anode/current collector interface from the anode/separator interface. We placed a layer of cellulose/graphene carbon composite aerogel (CCA) between the current collector and the anode (LCL-bottom). This layer works as a charge organizer that induces a high current density and encourages Li to deposit at the anode/current collector interface. Both in situ and ex situ images of the electrode demonstrate that the anode part of the cell has been flipped; with the newly deposited particles facing the current collector and the smooth surface facing the separator. The electrode in half and full cells showed outstanding cyclic stability and rate capability, with the LCL-bottom/LFP full cell capable of maintaining 94 % of its initial capacity after 1000 cycles.*

Introduction

The rapid growth of the electric vehicle (EV) market has attracted extensive research interest in developing the next-generation storage batteries that can meet the increasing demand for high power performance as well as high energy density and long cycle life. Lithium (Li) metal is often the choice of anode material because of its high theoretical capacity ($3860\ mAh\ g^{-1}$), low electrochemical potential (-3.040 V vs. standard hydrogen electrode) and low density ($0.534\ g\ cm^{-3}$).[1–6] However, there have been reports of serious safety hazards with the use of Li metal anodes.[7–11] A major reason for these problems appears to be the uncontrolled growth of Li dendrites that result in internal short circuits, thermal runaway, etc.[12–20]

Recently, several strategies, focusing on the modification of separator/anode interfaces, have been developed to inhibit the formation of Li dendrites and protect the separator. One strategy is to enhance the stability of the SEI by adjusting the electrolyte composition and additives.[21–27] These methods made with some success. However, most of the additives are continually consumed during cycling.[28,29] Another strategy of employing Li-C composites has attracted a great deal of attention.[30–35] For instance, a three-dimensional (3D) graphene/Ag aerogel was designed for Li metal anodes and significantly long cycle life in carbonate-based electrolytes. In this design, a conductive 3D porous architecture with a hierarchical pore structure accommodates deposited Li and ensures the integrity of the conductive network during cycling.[32] A self-supported TiC/C/Li anode was described by melting Li metal into TiC/C core/shell nanowire arrays, which may provide interspace for Li deposition and interconnected rapid electron transfer paths, leading to the effective growth of Li dendrites and lower interfacial resistance.[33] As stable and lightweight support for Li metal anodes, lithiophilic 3D nanoporous N-doped graphene was proposed to address the critical issues of uncontrolled dendrite growth and large volume change of Li anodes during the charging and discharging process.[34] A free-standing Li_xM/graphene foil (M = Si, Sn, or Al) with unique nanostructures was designed and exhibits stable cycling performance, which could avoid

[*] H. Mao, W. Yu, L. Liu, Y. Su, H. Kou, K. Xi, H. Zhao, X. Da, H. Wu, S. Ding
Xi'an Key Laboratory of Sustainable Energy Materials Chemistry, School of Chemistry, Xi'an Jiaotong University & Shaanxi Quantong Joint Research Institute of New Energy Vehicles Power, Xi'an Jiaotong University
Xi'an 710049 (China)
E-Mail: dingsj@mail.xjtu.edu.cn

Z. Cai, Y. Su
Collaborative Innovation Center of Chemistry for Energy Materials (iChEM), State Key Laboratory of Physical Chemistry of Solid Surfaces, and Department of Chemistry, College of Chemistry and Chemical Engineering, Xiamen University
Xiamen 361005 (China)

G. Liu, R. Wen
Key Laboratory of Molecular Nanostructure and Nanotechnology, Beijing National Laboratory for Molecular Sciences, CAS Research/Education Center for Excellence in Molecular Sciences, Institute of Chemistry, Chinese Academy of Sciences
Beijing 100190 (P. R. China)

B. Li
Department of Mechanical Engineering, University of Michigan-Dearborn
Dearborn, MI 48128 (USA)

W. Yan
Department of Environmental Science and Engineering, State Key Laboratory of Multiphase Flow in Power Engineering, Xi'an Jiaotong University
Xi'an 710049 (China)

Supporting information and the ORCID identification number(s) for the author(s) of this article can be found under: https://doi.org/10.1002/anie.202105831.

the intrinsic problems of volume expansion and dendrite growth.[35] These studies suggest that 3D Li-C composite anodes have the following advantages. First, the 3D hierarchical porous structure creates a large space for Li deposition and a continuous conductive network structure during the plating process, which ensures cycle stability. Second, the 3D conductive network homogenizes the current density distribution at the anode/separator interface, which is beneficial in suppressing the growth of Li dendrites to protect the separator. Third, 3D structures with a large specific surface area could provide abundant nucleate sites, which are useful in reducing the hysteresis voltage. Therefore, 3D Li-C composite anodes have alleviated dendrite formation and volume expansion problems to some extent. However, these designs are not effective in protecting the separator, from the dendrite growth at the anode/separator interface during cycling. Therefore, it is very important to design metallic Li anodes that decompress the anode/separator interface caused by dendrite growth.

Inspired by the above unique advantages of 3D Li-C composite anodes, we introduced a new strategy to suppress Li dendrite growth and volume change by transferring the main depositional interface to the anode/current collector interface from the anode/separator interface. Based on density functional theory calculations (DFT), it is more favorable for the Li to deposit on it rather than on the Li metal surface because of the relatively high current density distribution on CCA. As a result, dendrite formation always faces towards the current collector and not the separator. Even at the high current density of 25 mA cm^{-2} with a high stripping/plating capacity of 13 mAh cm^{-2}, the overpotential of LCL-bottom electrode still could maintain high cyclic stability within 50 mV for more than 300 h, compared with that of bare Li (overpotential of 1 V after about 50 h). And the capacity retention of LCL-bottom/LFP batteries could be significantly improved to > 94 % after 1000 cycles.

Results and Discussion

Experiment Design and Mechanism Analysis

CCA (cellulose/graphene carbon composite aerogel) was prepared by the sol-gel method described in our previous work.[36] A simple schematic illustration of preparation is shown in Figure S1and Figure S2. The 3D porosity of CCA is a result of the dual structure of the carbon network, where one-dimensional (1D) nanofibers are well stuck to the two-dimensional (2D) graphene flakes (Figure S3). Meanwhile, it has mechanical durability, flexibility, and excellent response to the pressure/release cycle (Figure S4 and S5). Next, we designed four different experimental models to evaluate anode performance. Based on the spatial position of Li electrode and CCA layer (LCL), the different models were: (i) a symmetrical cell with two Li disks and without CCA (LCL-without electrode); (ii) CCA was used as the interlayer, placed between the PP separator and Li metal anode (LCL-interlayer electrode); (iii) Li metal was melted and impregnated into CCA@ZnO (LCL-melting electrode) (Figure S6); and (iv) CCA was used as the current collector, placed on the bottom of the Li metal anode (LCL-bottom electrode).

Based on previous work,[6–10,32,36–39] mechanism analysis diagrams of LCL-without, LCL-interlayer, and LCL-melting electrodes are shown in Figure 1 a, b, and c, respectively. During the cycling of the Li metal electrode, the stripping/plating of Li ions occurs only at the anode/separator interface (Figure 1 a). Li deposition at a single interface would lead to vast volume expansion and subsequent Li dendrite growth upwards at the anode/separator interface caused by uneven current density distribution, which would puncture the separator and result in poor cyclability. To solve this problem, CCA was used as an interlayer, placed between the separator and Li metal anode. The mechanism analysis diagram of the LCL-interlayer electrode is shown in Figure 1 b. Li ions can uniformly nucleate and grow on the surface of the Li-anode, because of the fast electron transport channels and high surface area of the CCA. These provide homogeneous Li nucleation sites, and thus account for a lower overpotential compared to the pure Li electrode. As the cycle progresses, Li metal migrates up gradually, and continue with its original

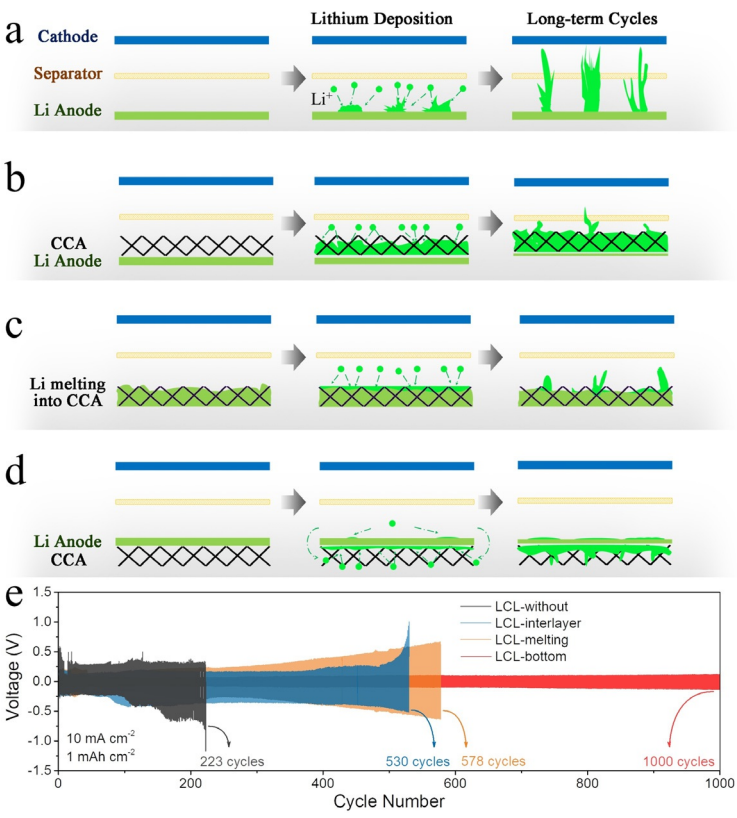

Figure 1. Mechanism analysis diagrams. a) Li metal without CCA (LCL-without). b) CCA as the interlayer (LCL-interlayer). c) Li metal melted into CCA@ZnO (LCL-melting). d) CCA placed on the bottom of the Li metal anode and used as the current collector (LCL-bottom). e) Voltage hysteresis of four different symmetrical batteries at 10 mA cm^{-2} with 1 mAh cm^{-2}.

formation of tip-like dendrites.[40,41] Therefore, the separator would still be punctured. As shown in Figure 1c, the LCL-melting electrode was prepared by melting Li metal into CCA@ZnO. During the Li stripping process, the Li metal in the electrode is stripped. Then, Li ions are deposited uniformly within the 3D conductive skeleton during the electrodeposition process. As the cell cycles, an increasing number of Li dendrites are deposited on the electrode surface, which causes the overpotential to increase and damage the separator. Better cycle stability is expected to be achieved. Based on the mechanism analysis diagrams of the other three strategies, the conjectural mechanism of the LCL-bottom electrode is shown in Figure 1d. When the layer is placed on the bottom of the Li metal, it can orientate Li deposition at the anode/current collector interface during the electrodeposition process. The main depositional interface transfers to the anode/current collector interface from the anode/separator interface by adjusting current density distribution, which is called Li dendrite „orientated-growth" strategy.

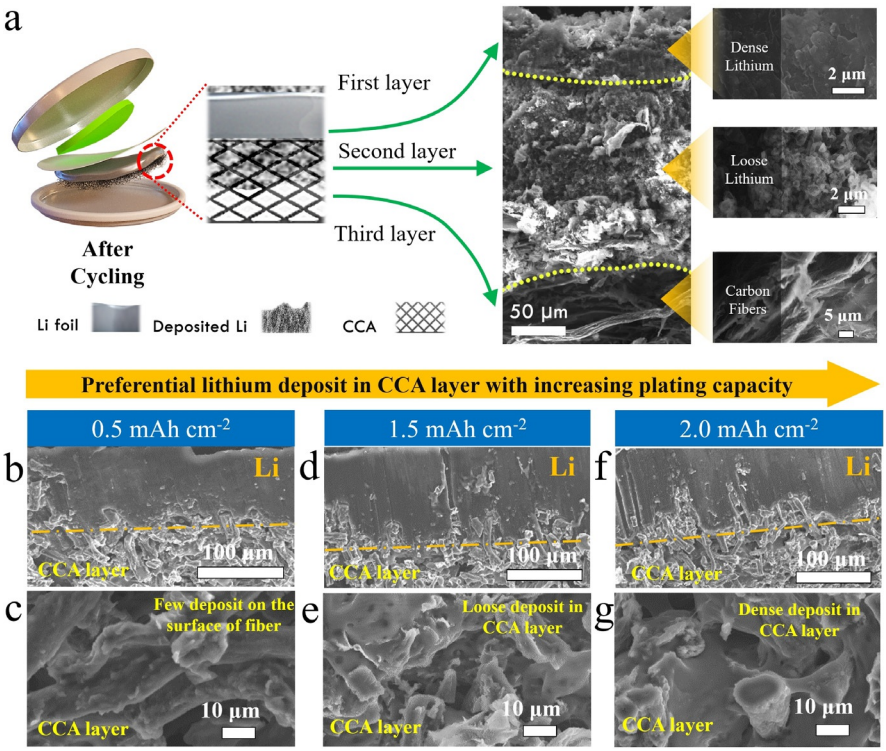

Figure 2. Cross-section SEM of Li metal anodes after 1000 cycles. a) Overall cross-sectional SEM image of LCL-bottom electrode. Li morphological evolution of the CCA layer on the LCL-bottom electrode. b, c) Li metal deposition after plating at 0.5 mAh cm^{-2}. d, e) Li metal deposition after plating at 1.5 mAh cm^{-2}. f, g) Li metal deposition after plating at 2.0 mAh cm^{-2}.

Next, this strategy was verified by the electrochemical behaviors of four different experimental schemes at a high current density of 10 mA cm^{-2} with 1 mAh cm^{-2}. It can be seen from Figure 1e that the LCL-bottom configuration shows the most stable cyclic performance and the lowest voltage hysteresis. The overpotential is approximately 118 mV after 1000 cycles (i.e., a high level; Table S1). The cycle lives of the LCL-without and LCL-interlayer batteries are less than 223 and 530 cycles, respectively. The LCL-melting configuration is slightly better with an overpotential of 617 mV after 578 cycles. It should be noted that the change in the nucleation overpotential with cycling is significantly lower for LCL-bottom electrode as compared with other configurations. This change is almost linear with cycling in the case of the LCL-melting electrode as can be concluded from Figure S7. The above electrochemical results support this strategy.

Morphology Characterization of Electrodes after Cycles

To further verify the dendrite growth mechanism of the strategy, the LCL-bottom battery was disassembled and analyzed after 1000 cycles. Cross-section SEM images of the LCL-bottom electrode (Figure 2a) show three different layers: a dense and smooth Li metal layer next to the separator, a loose layer of Li in the middle, and the 3D CCA layer near the current collector. No obvious cracks or holes can be observed in the first layer even after 1000 cycles, indicating low voltage hysteresis. Meanwhile, carbon fibers in the loose structure ensure continuous conductive paths, which is beneficial to cycle stability. In comparison, the symmetrical Li cell has only two distinguished layers after cycling: a loose layer with an obvious dendrite structure near the separator, and a dense layer near the current collector (Figure S8). After cycling, the dendrites would introduce numerous areas of „dead" Li and destroy the separator, which could lead to large voltage hysteresis and a short circuit of the battery. The Li morphology evolution of the CCA layer at different stages of deposition was determined from the SEM images after plating Li to 0.5 mAh cm^{-2} (Figure 2b, c), 1.5 mAh cm^{-2} (Figure 2d, e), 2.0 mAh cm^{-2} (Figure 2f, g), at a constant current density of 2.0 mA cm^{-2}. As the Li plating progresses, more Li can be observed deposited into the CCA layer. Hence, Li deposition occurs at the anode/current collector interface.

To further observe the dendrite growth of the anode/separator interface, the morphology of the anode was detected, as shown in Figure 3, after cycling at 10 mA cm^{-2} with 1 mAh cm^{-2}. After 223 cycles, the Li metal anode in the LCL-without electrode was dendritic and had a coarse surface (Figure 3a, b). Numerous tip-like dendrites would puncture the separator as a cause for serious safety concerns.[42] The LCL-interlayer electrode showed a more compact morphology when the CCA layer was placed between the separator and the anode. No obvious cracks were detected indicating

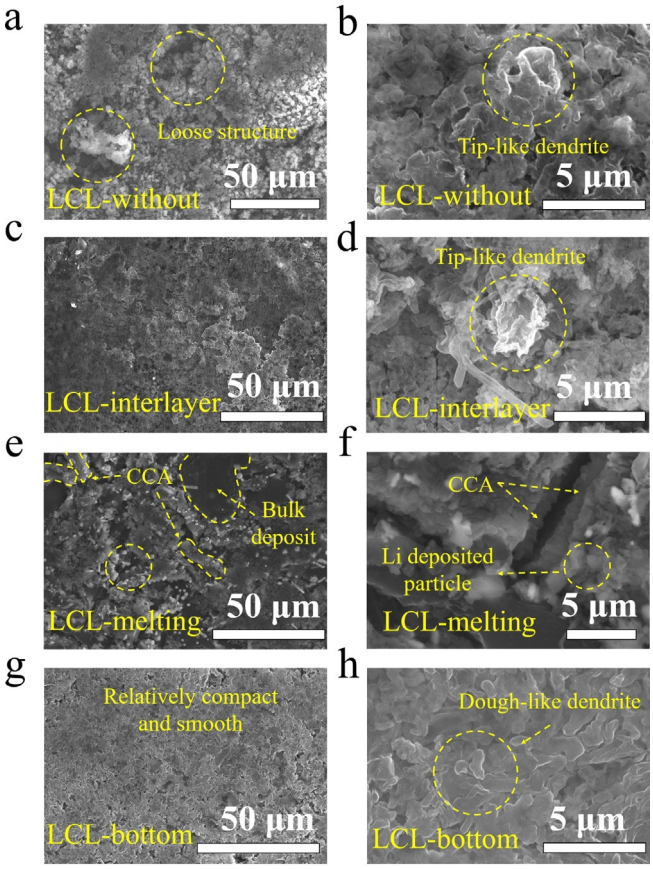

Figure 3. Post-cycling SEM characterization with 1 mAh cm^{-2} at 10 mA cm^{-2}. a, b) LCL-without morphology after 223 cycles. c, d) LCL-interlayer morphology after 530 cycles. e, f) LCL-melting morphology after 578 cycles with ≈617 mV of overpotential. g, h) LCL-bottom morphology after 1000 cycles with an overpotential of ≈118 mV.

the success of the CCA layer to buffer the volumetric changes (Figure 3c). Thus, the cell could be tested for 530 cycles. However, the Li deposits still migrate to the anode/separator interface during cycling (Figure S9). Finally, there were apparent tip-like dendrites on the surface (Figure 3d), which, could be held back to some degree by the CCA. But the inevitable separator penetration and „dead" Li introduction still killed the cell after 530 cycles. The LCL-melting electrode had more Li particles on the surface after cycling than LCL-interlayer electrode (Figure 3e, f). Several islands of dense bulk Li were observed on the surface of the D3 cell anode because of the improved adsorption of Li^+ on the Li metal covering the CCA backbone. Although dendrites were not prevalent on the surface, loose particles and the electrode cracks can still lead to capacity fading. Resulting in a cycle life only slightly better than that of LCL-interlayer electrode. When CCA was used as the current collector, even after 1000 cycles, the morphology of the LCL-bottom anode remained relatively compact and smooth (Figure 3g, h). The dough-like dendrites could not puncture the separator, ensuring long cycle life. The second-layer morphology of the LCL-bottom electrode was dendritic and loose (Figure S10). The results indicate that Li plating processes mainly occur at the anode/current collector interface, and few Li ions are deposited at the anode/separator interface. Therefore, the LCL-bottom morphology of the anode/separator interface is relatively smooth and compact, leading to excellent cycle stability at a high current density of 10 mA cm^{-2}. The strategy is supported by the above experimental results.

Electrochemical Performance of LCL-Bottom

As shown in Figure 4a, LCL-bottom electrodes display excellent cyclic stability for up to 405 h or 1460 cycles, with the overpotential increased to only 200 mV. Furthermore, LCL-bottom electrode possessed an excellent rate capability, which is much better than that of pure Li electrode (Figure 4b). Its overpotential increases from 23 to only 110 mV when the current density increases from 1 to 30 mA cm^{-2} at 1 mAh cm^{-2} fixed capacity. However, the voltage of pure Li increases from 73 mV to 322 mV with the current density increasing from 1 to 30 mA cm^{-2}. When the current density returns to 10 mA cm^{-2}, Li symmetric cell shows extremely poor stability compared to that of the LCL-bottom symmetric cell. As shown in Figure 4c, the LCL-bottom electrode could be kept stable for up to 2000 hours at 1 mA cm^{-2} with 4 mAh cm^{-2}; and the overpotential is just about 20 mV. Even as the current density reaching to 25 mA cm^{-2} with a high stripping/plating capacity of 13 mAh cm^{-2}, the overpotential of the LCL-bottom electrode could maintain excellent cyclic stability within 50 mV for more than 300 h, which is an improvement compared to that of bare Li (the voltage gradually increased to more than 1 V after about 50 h) (Figure 4d). The above results fully show the superiority of the „orientated-growth" strategy.

To explore the visibility of the LCL-bottom anode in practical applications, we tested it in a full cell configuration using a commercial $LiFePO_4$ (LFP) cathode. Figure 4d shows the cycling performance of the full cell as well as that of LFP/Li control cell for comparison. At 1 C, the initial capacities of LFP/Li and LFP/LCL-bottom were 168.15 and 166.46 mAh g^{-1}, respectively. After 450 cycles, the capacity of LFP/Li exhibited a downward trend with a coulombic efficiency (CE) below 90% (Figure S11) due to the formation of dendrites and breaking of the separator. The entire cycle life is shown in Figure S12a. In contrast, the capacity of the LFP/LCL-bottom cell could maintain a reversible capacity of 156.65 mAh g^{-1} (≈94% of its initial value) after 1000 cycles, with CE always >99% (i.e., a high level; Table S2). After 1200 cycles, the cells of LFP/Li (≈15% of its initial value) and LFP/LCL-bottom (≈92% of its initial value) were disassembled, and the bottom morphologies of the anodes were analyzed (Figure S12b, c, and d). As shown in Figure S12b, there were no visible changes on the bottom side of the Li anode of LFP/Li. However, the LCL-bottom anode bottom morphology changed dramatically (Figure S12c) to include numerous Li deposits in the CCA layer (Figure S12d). Even at a high current density (5 C), the capacity of LFP/LCL-bottom remained at 107.21 mAh g^{-1} with approximately 85% capacity retention after 1000 cycles, which is much better than the cycling stability of LFP/Li (approximately 43% capacity retention after 300 cycles). Meanwhile, the

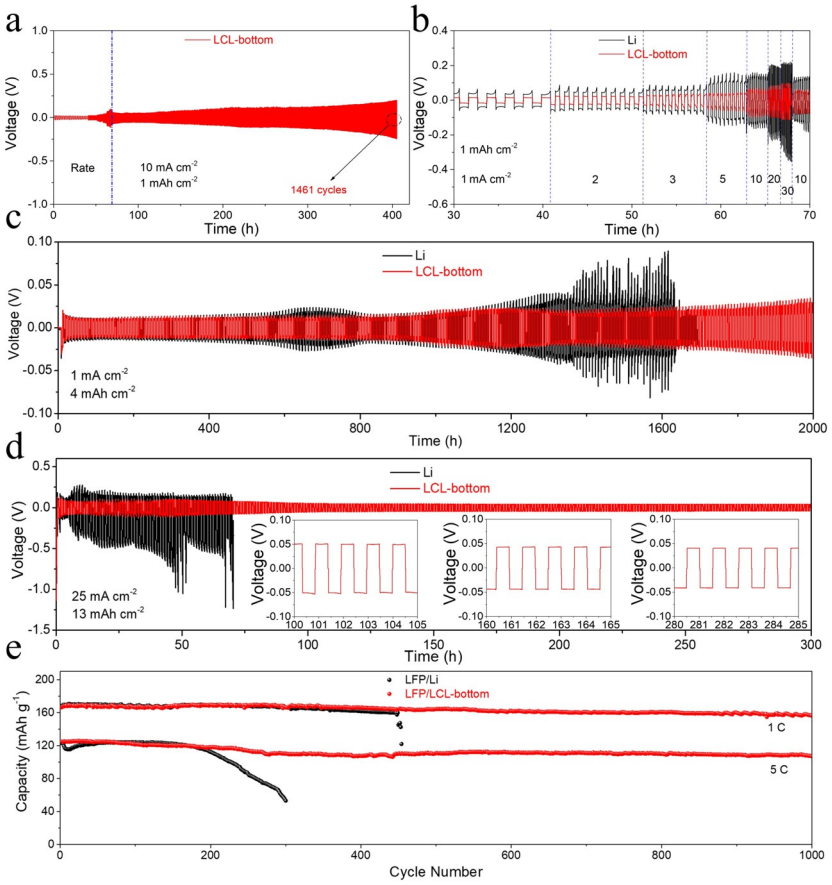

Figure 4. Cycling stability of Li plating/stripping. a) Rate performance and cycling stability of LCL-bottom electrode with 1 mAh cm^{-2} at a current density of 1, 2, 3, 5, 10, 20, 30, and 10 mA cm^{-2}. b) The rate performance of pure Li, LCL-bottom symmetric cells. Overpotential and stable voltage. c) At low current density of 1 mA cm^{-2} with 4 mAh cm^{-2}. d) At high current density of 25 mA cm^{-2} with 13 mAh cm^{-2}. e) Cycling behavior of cells that contain pure Li and LCL-bottom anodes with $LiFePO_4$ (LFP) cathode at 1 C and 5 C, respectively.

LFP/LCL-bottom full cell exhibits a small polarization voltage and outstanding cyclic performance with 9.6 mg LFP loading (Figure S13). Furthermore, the cycle performance of LCL-bottom with S cathode was tested at ≈7.0 mA cm^{-2} with 8.5 mg S loading (Figure S14). The areal capacity could maintain more than 4.0 mAh cm^{-2}, which is better than that of pure Li with S (fast decay to ≈1.2 mAh cm^{-2}). These results demonstrate the success of the strategy in transferring the main depositional interface to the anode/current collector interface from the anode/separator interface, leading to significant enhancement in the cycle life and the Li metal utilization efficiency.

We then explored whether commercial carbon cloth and carbon paper would also fit this strategy. To do this, we assembled three symmetrical cells using the configurations LCL-bottom, carbon cloth-Li, and carbon paper-Li symmetric cells. The other two carbon materials also showed relatively steady cycling performance after replacing CCA. As shown in Figure S15, the commercial carbon cloth-Li and carbon paper-Li electrodes could keep cycling up to 221 h (or 905 cycles) and 280 h (or 1146 cycles), respectively, until the nucleation overpotential reached ≈1.0 V. For longer cycling, LCL-bottom displayed a lower nucleation overpotential and a more stable voltage than the other two carbon materials. Nevertheless, with the two carbon materials, the overpotentials were still better than that of Li (60 h, 223 cycles). Commercial carbon paper and carbon cloth can also be used as lithium metal deposition sites (Figure S16). Therefore, this strategy is also suitable for both commercial carbon materials.

In Situ Characterization and DFT Calculations

In situ and non-destructive imaging characterization can directly visualize the morphological evolution and dynamic process from a cross-sectional perspective of Li metal anodes.[43] To form a deeper understanding of the mechanism of the dendrite „orientated-growth" mode, we focused on the structure and volume changes of Li symmetric batteries via in situ real-time optical microscope (OM) imaging of the cross-section observations. Figure 5a–c present the morphological evolution at the Li electrode/electrolyte interface (Video S1). Figure 5a shows an optical image of the Li anode at OCP (≈0.096 V). After holding potential at −0.1 V for 20 min, numerous black Li deposits appeared on the Li electrode, as shown in Figure 5b. Until 54 min, the thickness of the Li deposits greatly increased and the silvery-white Li electrode was almost covered, accompanied by a large volume change (Figure 5c). Figure 5d–f shows the morphological evolution at the LCL-bottom electrode/electrolyte interface (Video S2). At OCP (≈0.107 V), the electrode is distinctly displayed in Figure 5d. At −0.05 V for 60 min, and even at −0.1 V for 120 min, the electrode was still relatively stable with no obvious change at the interface, except for a small amount of Li deposition at the location marked with the red dotted circle (Figure 5e, f). The resolution loss at the Li/electrolyte interface of the videos and the figures is caused by the complex situation of the surface, like the bubble away from the observed cross-section (Figure S17). However, this loss is really limited and the anode/electrolyte interface can still be observed. The above OM results indicated that a small amount of Li metal was deposited at the LCL-bottom/electrolyte interface and the Li plating process mainly occurred in the CCA layer. The possible reason can be explained by the spots and rates of Li deposition that are mainly determined by R_s, R_{Li} and R_{ct}.[44,45] The smaller R_s, R_{Li}, and R_{ct} are, the greater the probability of Li deposition is. Figure S18 show a better conductivity of the LCL-bottom electrode than that of the Li electrode because of the CCA current collector. Therefore, the Li ions are more likely to deposit on the carbon layer.

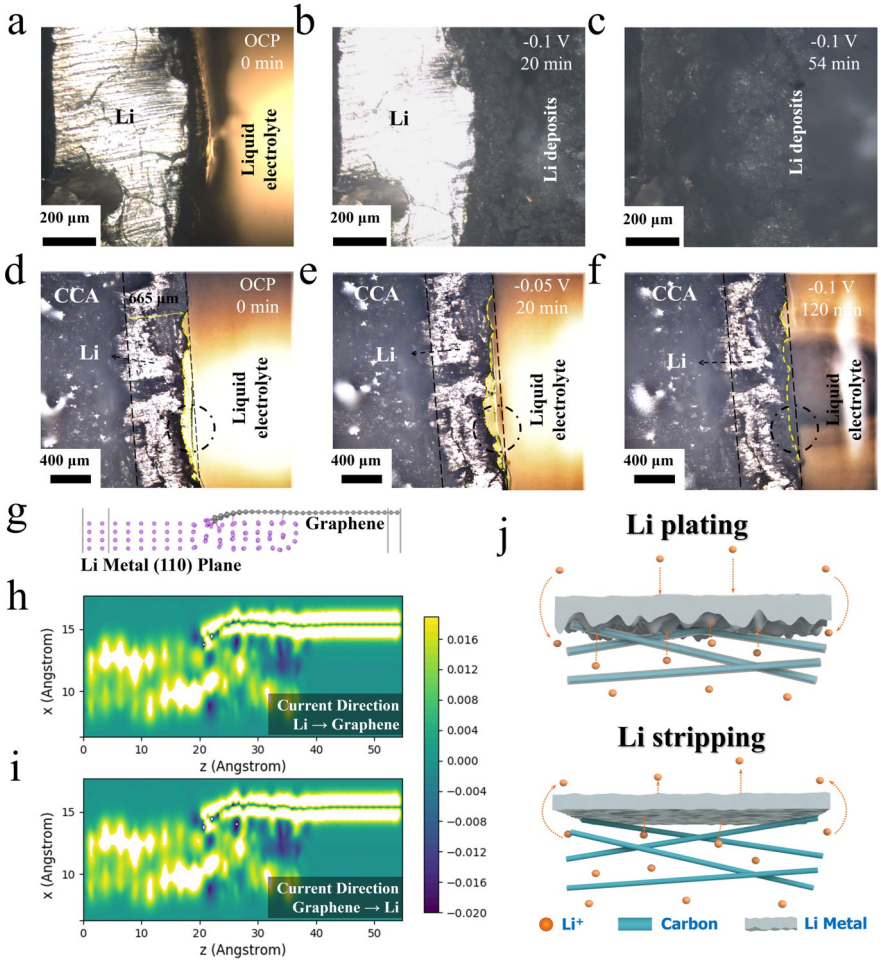

Figure 5. In situ characterization via real-time optical microscope (OM) imaging. a, b and c) Li morphology evolution at the anode/electrolyte interface upon Li deposition at −0.1 V for 54 min. d, e and f) Li morphology evolution of LCL-bottom electrode at the anode/electrolyte interface upon Li deposition at −0.05 V for 60 min and −0.1 V for another 60 min. g) The model contains a Li (110) surface with three atomic layers and a graphene monolayer. Color code: purple, Li; grey, C. The contour plots of the *z*-component of the linear response current density in the *x*−*z* plane in the case of h) from Li to graphene and i) from graphene to Li under a bias of 0.01 V. The simulation indicates that the current density is mainly distributed on the graphene layer under a bias of ±0.01 V. j) Local mechanism diagram of LCL-bottom electrode.

Here, an explanation is provided, which is the high current-density of CCA layer regulating lithium metal directional deposition. To further verify this hypothesis, explain the experimental results and shed more light on the mechanism of dendrite-oriented growth, we employed density functional theory (DFT) calculations of the charge density. Since graphene is coated on the surface of carbon fibers in CCA, we focused our calculation on the graphene-Li model. We considered two cases based on LCL-interlayer and LCL-bottom electrodes, which led to the Li-graphene (Figure S19a) and the graphene-Li cluster (Figure S19b). The simulation indicates that the charge density is mainly distributed on graphene over Li in either case, which explains the experimental results that showed the CCA layer as preferential locations for Li deposition. The current density distribution was further determined by DFT calculations of the current density implemented in the QuantumWise Atomisix Toolkit (ATK). As shown in Figure 5g, the model contains a Li (110) surface with three atomic layers and a graphene monolayer. The distance between the Li (110) surface and graphene is in the range of 1.8–2.3 Å. The current incident from the right (from the graphene side) gets transmitted through the device. The current density in the graphene layer shows a symmetry corresponding to carbon π-electrons carrying the current. The current density in the lithium surface drops at the boundary between the lithium atoms bonded to the graphene surface and the non-bonded lithium atoms. And the simulation indicates that the current density is mainly distributed on the graphene layer under a bias of ±0.01 V (Figure 5h, i), which is in accordance with the experimental observation. The high current density in the carbon layer makes it more favorable for deposition. Therefore, this novel strategy makes the main depositional interface transfer to the anode/current collector interface from the anode/separator interface.

From the above results, the local mechanism diagram of the LCL-bottom electrode is shown in Figure 5j. The entire electrode is surrounded by electrolyte, like a connector. Li ions can migrate through the edge of the electrode. With the Li stripping process, Li ions move to the cathode. Because of the concentration gradient, Li ions in the carbon layer will migrate through the edge of the LCL-bottom electrode. With the Li plating process, Li ions move to the anode. And they can migrate to the carbon layer through the edge of the electrode due to the concentration gradient. Meanwhile, most Li ions obtain electrons from the CCA current collector and deposit preferentially, with a few deposition processes happening. As shown in Figure S20, at the beginning of Li deposition, Li ions obtain electrons on the surface of the current collector, forming a larger Li nucleus at the anode/current collector interface of the LCL-bottom electrode, as well as minimal nuclei at the anode/separator interface. The result indicates that the rate of Li deposition at the anode/current collector interface is much higher than that of the anode/electrolyte interface. There is enough evidence to support this innovative strategy, and we believe that it will leapfrog the development for LMBs.

Conclusion

In conclusion, we introduced a novel and universal approach to address the dendrite formation phenomenon in LMBs. It is based on transferring the main Li depositional interface to the anode/current collector interface from the anode/separator interface through a facile method: placing a CCA layer between the current collector and the Li metal anode. Ex situ experiments and in situ real-time OM imaging were used to exhibit that the anode part of the cell has been flipped; with the new deposited particles facing the current collector and smooth surface facing the separator. The above advantages could well protect the separator and ensure the LFP full cell an outstanding cyclic performance with a capacity retention of 94 % after 1000 cycles. Furthermore, DFT calculations suggest that the current density in the CCA layer is higher than that of at the lithium surface, which makes CCA layer more favorable for the deposition. In other words, less depositions at the anode/separator interface. Therefore, this method can effectively protect both the electrode and the separator and consequently enhance the cyclic stability of the LMBs. We believe that this work can encourage further studies for the degradation mechanism of lithium metal anode and enable a promising anode.

Acknowledgements

This research was supported by the National Natural Science Foundation of China (No. 51773165, 51973171), Natural Science Foundation of Shaanxi Province (2020JC-09), Key Laboratory Construction Program of Xi'an Municipal Bureau of Science and Technology (201805056ZD7CG40), China Postdoctoral Science Foundation (2019M663687), Fundamental Research Funds for the Central Universities (xjh012020042). The authors would like to thank the Center for Advancing Materials Performance from the Nanoscale (CAMP-Nano) for allowing the use of field-emission scanning electron microscopy.

Conflict of Interest

The authors declare no conflict of interest.

Stichwörter: anode/separator interface · depositional interface transfer · lithium metal battery · long cycles

[1] M. Armand, J. M. Tarascon, *Nature* **2008**, *451*, 652 – 657.
[2] M. S. Whittingham, *Chem. Rev.* **2014**, *114*, 11414 – 11443.
[3] B. Liu, J. G. Zhang, W. Xu, *Joule* **2018**, *2*, 833 – 845.
[4] X. G. Han, Y. H. Gong, K. Fu, X. F. He, G. T. Hitz, J. Q. Dai, A. Pearse, B. Liu, H. Wang, G. Rubloff, Y. Mo, V. Thangadurai, E. D. Wachsman, L. Hu, *Nat. Mater.* **2017**, *16*, 572 – 580.
[5] D. C. Lin, Y. Y. Liu, Y. Cui, *Nat. Nanotechnol.* **2017**, *12*, 194 – 206.
[6] P. Shi, X. Q. Zhang, X. Shen, R. Zhang, H. Liu, Q. Zhang, *Adv. Mater. Technol.* **2020**, *5*, 1900806.
[7] G. X. Li, Z. Liu, Q. Q. Huang, Y. Gao, M. Regula, D. W. Wang, L. Q. Chen, D. H. Wang, *Nat. Energy* **2018**, *3*, 1076 – 1083.
[8] Y. Zhang, W. Luo, C. W. Wang, Y. J. Li, C. J. Chen, J. W. Song, J. Q. Dai, E. M. Hitz, S. Xu, C. Yang, Y. Wang, L. Hu, *Proc. Natl. Acad. Sci. USA* **2017**, *114*, 3584 – 3589.
[9] Y. Zhang, T. T. Zuo, J. Popovic, K. Lim, Y. X. Yin, J. Maier, Y. G. Guo, *Mater. Today* **2020**, *33*, 56 – 74.
[10] X. B. Cheng, R. Zhang, C. Z. Zhao, Q. Zhang, *Chem. Rev.* **2017**, *117*, 10403 – 10473.
[11] K. Shen, Z. Wang, X. Bi, Y. Ying, D. Zhang, C. Jin, G. Hou, H. Cao, L. Wu, G. Zheng, Y. Tang, X. Tao, J. Lu, *Adv. Energy Mater.* **2019**, *9*, 1900260.
[12] Y. S. Cohen, Y. Cohen, D. Aurbach, *J. Phys. Chem. B* **2000**, *104*, 12282 – 12291.
[13] Y. P. Guo, H. Q. Li, T. Y. Zhai, *Adv. Mater.* **2017**, *29*, 1700007.
[14] X. W. Sun, X. Y. Zhang, Q. T. Ma, C. Z. Guan, W. Wang, J. Y. Luo, *Angew. Chem. Int. Ed.* **2020**, *59*, 6665 – 6674; *Angew. Chem.* **2020**, *132*, 6730 – 6739.
[15] X. Y. Zhang, A. X. Wang, X. J. Liu, J. Y. Luo, *Acc. Chem. Res.* **2019**, *52*, 3223 – 3232.
[16] R. Bouchet, S. Maria, R. Meziane, A. Aboulaich, L. Lienafa, J. P. Bonnet, T. Phan, D. Bertin, D. Gigmes, D. Devaux, R. Denoyel, M. Armand, *Nat. Mater.* **2013**, *12*, 452 – 457.
[17] J. M. Doux, H. Nguyen, D. Tan, A. Banerjee, X. F. Wang, E. A. Wu, C. H. Jo, H. D. Yang, Y. S. Meng, *Adv. Energy Mater.* **2020**, *10*, 1903253.
[18] H. F. Yan, H. C. Wang, D. H. Wang, X. Li, Z. L. Gong, Y. Yang, *Nano Lett.* **2019**, *19*, 3280 – 3287.
[19] X. Li, Z. H. Ren, M. N. Banis, S. X. Deng, Y. Zhao, Q. Sun, C. Wang, X. Yang, W. Li, J. Liang, X. Li, Y. Sun, K. Adair, R. Li, Y. Hu, T.-K. Sham, H. Huang, L. Zhang, S. Lu, J. Luo, X. Sun, *ACS Energy Lett.* **2019**, *4*, 2480 – 2488.
[20] Q. Zhang, D. X. Cao, Y. Ma, A. Natan, P. Aurora, H. L. Zhu, *Adv. Mater.* **2019**, *31*, 1901131.
[21] G. Wang, C. Chen, Y. H. Chen, X. W. Kang, C. H. Yang, F. Wang, Y. Liu, X. H. Xiong, *Angew. Chem. Int. Ed.* **2020**, *59*, 2055 – 2060; *Angew. Chem.* **2020**, *132*, 2071 – 20761.
[22] G. J. Xu, X. H. Shangguan, S. M. Dong, X. H. Zhou, G. L. Cui, *Angew. Chem. Int. Ed.* **2020**, *59*, 3400 – 3415; *Angew. Chem.* **2020**, *132*, 3426 – 3442.
[23] H. J. Yang, A. Naveed, Q. Y. Li, C. Guo, J. H. Chen, J. Y. Lei, J. Yang, Y. N. Nuli, J. L. Wang, *Energy Storage Mater.* **2018**, *15*, 299 – 307.
[24] X. Cao, X. D. Ren, L. F. Zou, M. H. Engelhard, W. Huang, H. S. Wang, B. E. Matthews, H. Lee, C. Niu, B. W. Arey, Y. Cui, C. Wang, J. Xiao, J. Liu, W. Xu, J.-G. Zhang, *Nat. Energy* **2019**, *4*, 796 – 805.
[25] G. X. Li, Y. Gao, X. He, Q. Q. Huang, S. R. Chen, S. H. Kim, D. H. Wang, *Nat. Commun.* **2017**, *8*, 850.
[26] J. M. Zheng, M. H. Engelhard, D. H. Mei, S. H. Jiao, B. J. Polzin, J. G. Zhang, W. Xu, *Nat. Energy* **2017**, *2*, 17012.
[27] G. X. Li, Q. Q. Huang, X. He, Y. Gao, D. W. Wang, S. H. Kim, D. H. Wang, *ACS Nano* **2018**, *12*, 1500 – 1507.
[28] W. Li, H. B. Yao, K. Yan, G. Y. Zheng, Z. Liang, Y. M. Chiang, Y. Cui, *Nat. Commun.* **2015**, *6*, 7436.
[29] Y. Lu, Z. Tu, L. Archer, *Nat. Mater.* **2014**, *13*, 961 – 969.
[30] X. Ji, D. Y. Liu, D. G. Prendiville, Y. C. Zhang, X. N. Liu, G. D. Stucky, *Nano Today* **2012**, *7*, 10 – 20.
[31] A. Kozen, C. F. Lin, A. J. Pearse, M. A. Schroeder, X. G. Han, L. B. Hu, S. B. Lee, G. W. Rubloff, M. Noked, *ACS Nano* **2015**, *9*, 5884 – 5892.
[32] Y. Yang, M. Zhao, H. B. Geng, Y. F. Zhang, Y. X. Fang, C. C. Li, J. B. Zhao, *Chem. Eur. J.* **2019**, *25*, 5036 – 5042.
[33] S. F. Liu, X. H. Xia, Y. Zhong, S. J. Deng, Z. J. Yao, L. Y. Zhang, X.-B. Cheng, X. Wang, Q. Zhang, J. Tu, *Energy Mater.* **2018**, *8*, 1702322.

[34] G. Huang, J. H. Han, F. Zhang, Z. Q. Wang, H. Kashani, K. Watanabe, M. W. Chen, *Adv. Mater.* **2019**, *31*, 1805334.
[35] J. Zhao, G. M. Zhou, K. Yan, J. Xie, Y. Z. Li, L. Liao, Y. Jin, K. Liu, P.-C. Hsu, J. Wang, H.-M. Cheng, Y. Cui, *Nat. Nanotechnol.* **2017**, *12*, 993 – 999.
[36] H. Mao, L. M. Liu, L. Shi, H. Wu, J. X. Lang, K. Wang, T. Zhu, Y. Gao, Z. Sun, J. Zhao, G. Gao, D. Zhang, W. Yan, S. Ding, *Sci. Bull.* **2020**, *65*, 803 – 811.
[37] D. Zhang, A. Dai, M. Wu, K. Shen, T. Xiao, G. Hou, J. Lu, Y. Tang, *ACS Energy Lett.* **2020**, *5*, 180 – 186.
[38] J. F. Zhu, J. Chen, Y. Luo, S. Q. Sun, L. G. Qin, H. Xu, P. Zhang, W. Zhang, W. Tian, Z. Sun, *Energy Storage Mater.* **2019**, *23*, 539 – 546.
[39] W. Deng, W. H. Zhu, X. F. Zhou, X. Q. Peng, Z. P. Liu, *ACS Appl. Mater. Interfaces* **2018**, *10*, 20387 – 20395.
[40] Y. Deng, H. Lu, Y. Cao, B. Xu, Q. Hong, W. Cai, W. Yang, *J. Power Sources* **2019**, *412*, 170 – 179.
[41] L.-L. Kong, Z. Zhang, Y.-Z. Zhang, S. Liu, G.-R. Li, X.-P. Gao, *ACS Appl. Mater. Interfaces* **2016**, *8*, 31684 – 31694.
[42] J. Liu, Z. N. Bao, Y. Cui, E. J. Dufek, J. B. Goodenough, P. Khalifah, Q. Li, B. Y. Liaw, P. Liu, A. Manthira, Y. S. Meng, V. R. Subramanian, M. F. Toney, V. V. Viswanathan, M. S. Whittingham, J. Xiao, W. Xu, J. Yang, X.-Q. Yang, J.-G. Zhang, *Nat. Energy* **2019**, *4*, 180 – 186.
[43] Y. X. Song, Y. Shi, J. Wan, S. Y. Lang, X. C. Hu, H. J. Yan, B. Liu, Y.-G. Guo, R. Wen, L.-J. Wan, *Energy Environ. Sci.* **2019**, *12*, 2496 – 2506.
[44] H. Liu, X. B. Cheng, R. Xu, X. Q. Zhang, C. Yan, J. Q. Huang, Q. Zhang, *Adv. Energy Mater.* **2019**, *9*, 1902254.
[45] J. Pu, J. C. Li, K. Zhang, T. Zhang, C. W. Li, H. X. Ma, J. Zhu, P. V. Braun, J. Lu, H. Zhang, *Nat. Commun.* **2019**, *10*, 1896.

Manuskript erhalten: 29. April 2021
Veränderte Fassung erhalten: 28. Mai 2021
Akzeptierte Fassung online: 6. Juni 2021
Endgültige Fassung online: 19. Juli 2021

